Cell, Volume *132*

Structural Basis of Membrane Invagination by F-BAR Domains

Adam Frost, Rushika Perera, Aurélien Roux, Krasimir Spasov, Olivier Destaing, Edward H. Egelman, Pietro De Camilli, and Vinzenz M. Unger

Supplemental Experimental Procedures

F-BAR Domain Purification and Mutagenesis

cDNA fragments encoding human FBP17 (1-303) and CIP4 (1-284) were subcloned into pGEX6P-1 (Amersham Biosciences, Piscataway, NJ) with codons for six additional histidine residues inserted at the C-terminus via PCR. Fusion proteins were bacterially expressed and purified first on a nickel affinity resin and then on a GST-glutathione affinity column. The GST tag was cleaved using PreScission protease (Amersham Biosciences, Piscataway, NJ), followed by gel filtration chromatography (Superdex 200 10/300 GL; Amersham Pharmacia Biosciences) in buffer containing (350 mM NaCl/250mM Imidazole/20mM HEPES/1 mM DTT, pH 7.4). Aliquots of 1-3 mg/ml protein were stored at -80° C. Site-directed mutation of select residues was performed via the quick-change protocol (Stratagene, La Jolla, CA).

Liposome Preparation and Membrane Binding and Tubulation *in vitro*

Synthetic lipids in chloroform were purchased from Avanti Polar Lipids and combined in mixtures composed of 85% mol./mol. phospholipids and 15% mol./mol. cholesterol. Lipids were dried under a stream of argon with gentle vortexing in glass vials, redissolved in absolute hexane, dried with argon again, and dessicated under high-

vacuum for one hour. Lipids were then hydrated with buffer (50mM KCl/10mM HEPES/1mM DTT, pH 7.4), sonicated, subjected to 10 cycles of freeze-thaw, and used immediately or stored in aliquots at -80° C (see Figure S9).

All of the results reported here, except for the mutant analysis reported below, were obtained using a synthetic phospholipid mixture that included 10% brain phosphatidyl-ethanolamine (PE), 5% liver phospho-inositides (PI), 50% palmitoyl-oleyl phosphatidyl-serine (POPS), and 35% palmitoyl-oleyl phosphatidyl-choline (POPC). Similar results, although not explicitly presented here, were also seen with synthetic phospholipid mixtures that included 20-30% brain phosphatidylethanolamine (PE), 5% liver phosphoinositides (PI), 30-40% palmitoyl-oleyl phosphatidylserine (POPS), and 35% palmitoyl-oleyl phosphatidylcholine (POPC). Finally, some of the mutants studied here (F117D in particular) only formed tubes when using liposomes composed of pure 16:0/18:1 phosphatidyl-serine (POPS). Therefore, quantitative comparisons of wild type with mutant proteins were performed after incubation with equivalent amounts of pure POPS (see below).

Liposomes (0.1 – 0.25 mg/ml) were equilibrated at 30°C (tubules) or 2°C (2D crystals) for 1 hour before adding F-BAR domains at a lipid-to-protein ratio of 2:1 mass/mass. The ability of the F-BAR domain to bind phospholipids is sensitive to salt concentration, hence protein aliquots in high salt buffers were diluted >5-fold into ddH_20, or protein+liposome mixtures were dialyzed against a low salt buffer overnight (50mM KCl/10mM HEPES/1mM DTT, pH 7.4) with similar results. Well-ordered helical lattices were obtained after a period of slow cooling following tubule formation at

30°C. An annealing curve programmed into a PCR machine cooled the sample by 5 degrees per hour, each followed by 5 minutes of 1 degree warming, such that after 7 hours the sample was at 2°C. This annealing procedure was only used for generating samples for cryo(electron) imaging and structure determination, and was shown to have negligible effects on the morphology of protein-free liposomes (Figure S9). In contrast, obtaining 2D lattices with the wild-type protein required that the lipids never be warmer than 4°C after exposure to the protein. Comparisons of mutant and wild type protein function were performed with protein samples that were purified on the same day in the same buffers and matched in concentration as assayed by SDS-PAGE and Bradford assays. To avoid bias, quantification of tubule forming ability was measured while blinded to the identity of the protein. Tubule number and length were measured with NIH ImageJ (http://rsb.info.nih.gov/ij/).

Electron Microscopy

2D and helical arrays were screened and where applicable, single-axis tilt series were acquired, using 1% uranyl acetate-stained samples and a Philips Tecnai 12 microscope operating at 120 kV. To vitrify samples for cryomicroscopy, holey carbon grids were glow discharged in the presence of air, sample was applied to the grid in a cold room, and excess liquid was blotted off for 4 sec before plunging into liquid ethane. Images were taken at a sample temperature of –172°C under low-dose conditions on a Philips Tecnai F20 microscope equipped with a field emission gun and operating at an accelerating voltage of 160-200 kV, nominal magnifications of 29-50kx, and defocus values of –1,500 to –22,000 Å. Images were recorded on either Kodak SO-163 film and developed for 12

min in a full-strength Kodak D19 developer (YALE) or on a GATAN 4kx4k CCD (NRAMM, Scripps Research Institute). The parameters for correction of the contrast transfer function were estimated with ACE as shown in Figure S2C (Mallick et al., 2005).

2D Crystal Image Processing

Images of 2D crystals were corrected for lattice distortions, effects of the contrast transfer function, and astigmatism using the MRC image-processing software package (Crowther et al., 1996; Smith, 1999). Two rounds of "unbending" with a Gaussian-profile maskhole were employed, with reference areas of 10% and 5% of total pixel area used in the first and second rounds, respectively. Due to the marked asymmetry of the unit cell, quantifying the anisotropy in the auto-correlation peak improved the cross-correlation map. The program ALLSPACE was used to determine whether any images of negatively stained or vitrified crystals possessed a two-dimensional plane group symmetry, see Table S1 (Valpuesta et al., 1994). No symmetry could be found in any of the images, and attempts to average data from multiple images in reciprocal space yielded unacceptable phase residuals. Consequently, a single-axis tilt series including 13 images from ±40° of a single negatively stained crystal was acquired. For the images of the more highly tilted crystals, the tilt angle calculated with the program EMTILT was within <1° of the nominal goniometer settings (Shaw and Hills, 1981). Applying the proper tilt geometry, all 13 images were brought to their common phase origin, merged and subjected to an additional round of origin and geometry refinement against the preliminary 3D-model obtained after fitting of the lattice lines. After fitting a final set of lattice lines (Figure S8) the projection structure (Figure 7C) was then calculated out of the 3D-data set using a B-

factor of B=-5000Å^{-2}.

Helical Image Processing

Fourier–Bessel reconstruction proved to be limited in recovering high resolution features from the large, hollow helical arrays because of flexibility and multiple image interpolations required for axis alignment and straightening. Moreover, helices with the same apparent diameter proved to have distinct helical symmetries, precluding reciprocal space averaging. We therefore reconstructed individual tubes with an extended version of the Iterative Helical Real Space Reconstruction (IHRSR) single particle algorithm as implemented in SPIDER (Egelman, 2000; Frank et al., 1996). Modifications to the procedure included the use of low-resolution Fourier-Bessel reconstructions as starting models (Figure S3A-B); initial rounds of projection matching performed with layer-line filtered images to enhance the SNR for the helical symmetry search; searching for continuous, but smoothly varying, out-of-plane tilt to identify short-range bending in the direction perpendicular to the tube's long axis (Figure S2D) and 3D CTF correction with Wiener filtering using the frequency-dependent spectral signal-to-noise ratio as determined in SPIDER (Frank et al., 1996; Pomfret et al., 2007). Each reconstruction is based on 1,200-2,400 segments, each 75 nm long with an overlap of 73 nm. The total number of unique F-BAR dimers contributing to the reconstructions ranged from ~1500 to ~3000 and the highest resolution was achieved from images of tubules with an inherent two-fold rotational symmetry, C_n=2, around the cylindrical axis (Figure S3C-D). Handedness was confirmed by analysis of images acquired after tilting the specimen relative to the imaging plane. Surface renderings were created with UCSF Chimera

(Pettersen et al., 2004) and CCP4MG (Potterton et al.). Evolutionary conservation scores and surface mapping were determined with Consurf (Landau et al., 2005). Resolution estimates were calculated *ab inito* with RMEASURE (Sousa and Grigorieff, 2007). Helical arc lengths along the left-handed path defined by the lateral interactions were calculated according to: $s = \sqrt{R^2 + \left(\frac{\Delta z}{\Delta \theta}\right)^2} \bullet (\Delta \theta)$, where R is the radius, Δz and $\Delta\theta$ are the experimentally determined rise and twist for this periodicity, respectively.

Cell culture, transfection and reagents

COS7 cells (ATCC, Rockville, MD) were cultured at 37°C and 5% CO_2 in Dulbecco's modified Eagle's medium supplemented with 10% fetal bovine serum. FBP17-GFP, mRFP-FBP17 and Amphiphysin2-GFP have all been previously described (Itoh et al., 2005). GFP- and mRFP-tagged proteins were co-expressed in COS7 cells by transfecting 1-3μg DNA using the Amaxa nucleofector kit (Amaxa, Cologne, Germany). Cells were seeded in glass-bottomed 35mm dishes (Mattek Corporation, Ashland, MA) and imaged approximately 14-24 hours later (50-70% confluency). For immunofluorescence, cells were grown on coverslips, fixed with 4% formaldehyde (freshly prepared from parafomaldehyde), and processed by standard procedures.

Live Cell Microscopy

Prior to imaging, medium was replaced with an imaging buffer containing 136mM NaCl, 2.5mM KCl, 2mM $CaCl_2$, 1.3mM $MgCl_2$, 10mM HEPES at pH 7.4. Cells were imaged at 37°C using a spinning-disk confocal system (Perkin Elmer, Waltham, MA), mounted

onto an IX-71 inverted microscope (Olympus, Melville, NY), equipped with a 1Kb x 1Kb, Hamamatsu EM-CCD camera (Hamamatsu, Hamamatsu City, Japan). Samples were imaged using a 100X oil objective, yielding a spatial resolution of 0.1 μm/pixels. Excitation was achieved using 488 argon and 568 argon/krypton lasers (Melles Griot, Carlsbad, CA). Exposure times were between 0.2-0.6 seconds. NIH Image J and/or iQ software was used to process raw images.

Video-DIC and Determination of Persistence Lengths

The formation of lipid sheets and video-DIC imaging of protein-induced tubulation was performed according to (Itoh et al., 2005; Roux et al., 2006). Briefly, membrane preparations were placed on the stage of an Axiovert 200 ZEISS (Germany) microscope for observation at room temperature with a JAI Pulnix (USA) TM1400CL camera and DVR software (Advanced Digital Vision Inc. USA). FBP17, amphiphysin and dynamin containing solutions were applied to one side of the chamber and the deformation of membrane sheets produced by its diffusion into the chamber was recorded at normal video rate (30 fps) with 1300x1024 resolution under Differential Interference Contrast (DIC) settings. For each tubule, positions of the tip and the base were tracked using the manual tracking plugin with NIH ImageJ (http://rsb.info.nih.gov/ij/). This procedure was repeated for one hundred sequential frames for each tubule, and the tip-to-base distance was extracted for each frame. Each data point is the rms^2 (root mean square to the square) for all of the tip-to-base measurements for a given tubule. The rms^2 were plotted against the total length and the theoretical curve fit to the data derives from the following equation: $\delta R^2(t) = 2(L_p)^2[x/L_p - 1 + e^{(-x\ Lp)}]$; where $\delta R^2(t)$ is the rms^2, x the total length and

L_p the persistence length (Derenyi et al., 2002; Le Goff et al., 2002a; Le Goff et al., 2002b).

Wide-Angle X-Ray Scattering

Liposomes at 20mg/ml were sealed into thin-walled glass capillaries that were thermally equilibrated at 30°C or 4°C for 30 minutes before data acquisition. X-ray diffractograms were recorded with an image plate mounted on a sealed-tube Rigaku R-Axis IIC operating at 50 kV and 100 mA. The x-ray beam was filtered for CuKα radiation using a Ni foil. Diffraction patterns were recorded at each temperature for 10 to 30 min.

Thin Section TEM

COS7 cells were fixed with either 1.3% glutaraldehyde in 66mM sodium cacodylate buffer or 2% glutaraldehyde in a buffer containing 30mM Hepes-NaOH (pH 7.4), 100mM NaCl, 2.5mM $CaCl_2$. Subsequently, they were post-fixed with 1% OsO_4 in 1.5% $K_4Fe(CN)_6$ and 0.1M sodium cacodylate, en bloc stained with 0.5% uranyl magnesium acetate, dehydrated and embedded in Embed 812. Sections were imaged in a Philips Tecnai 12 operating at 120 kV. Electron microscopy reagents were purchased from Electron Microscopy Sciences (Hatfield, PA).

Figure S1: Experimental versus Model 2D Fourier Transforms.

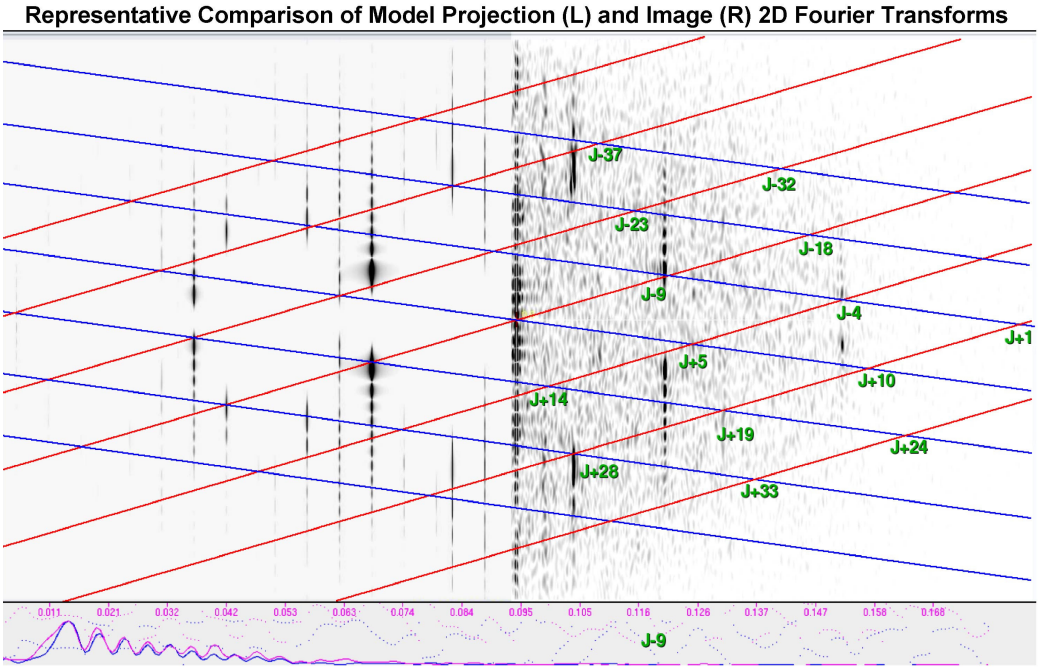

Right: Fourier transform of the aligned, straightened tubule overlaid with the lattice and annotated with the Bessel function orders used for a preliminary Fourier-Bessel reconstruction. Left: Fourier transform of a 2D projection image calculated from a helical reconstruction, overlaid with the same lattice. Bottom: Amplitude (continuous) and Phase (dotted) modulation of pixels values along the layerline corresponding with the J-9 Bessel function from the experimental (right) image data. The phase modulations for the near and far sides of the function are precisely 180° out of phase with each other, consistent with the assignment of an odd Bessel order. Analysis performed with SUPRIM and PHOELIX (Schroeter and Bretaudiere, 1996; Whittaker et al., 1995).

Figure S2: Resolution Comparison, Representative Electron (Cryo)Micrograph, Determination of CTF and Out-of-Plane Tilt

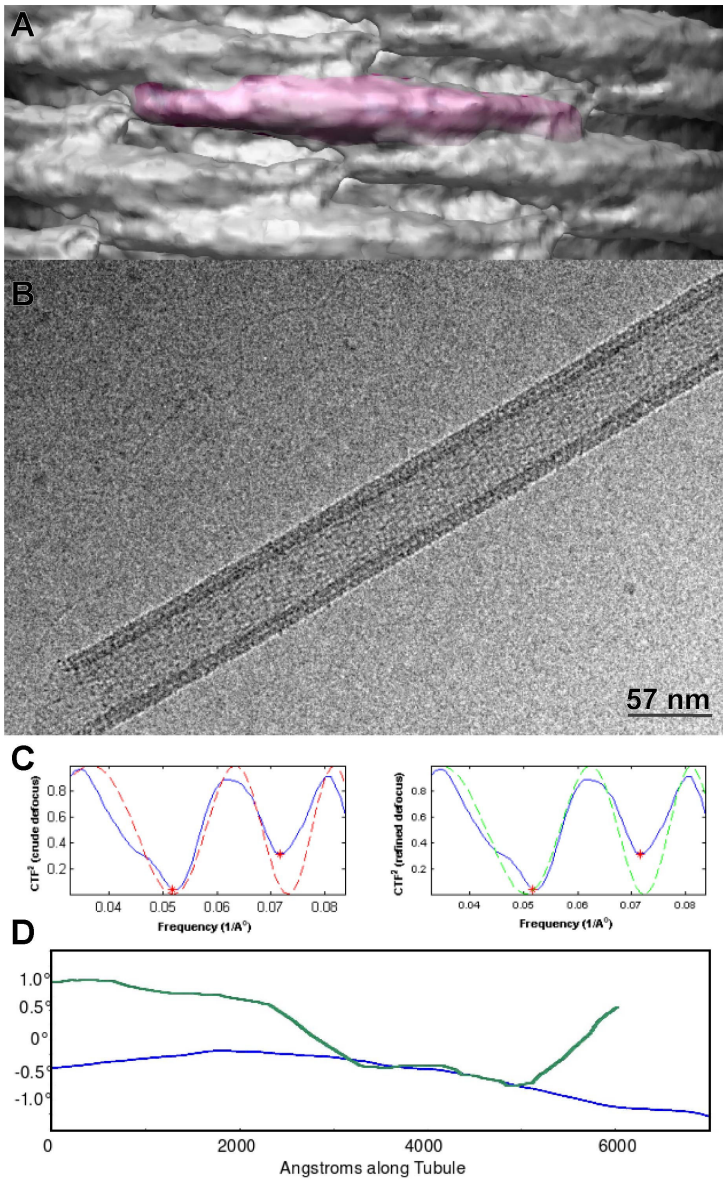

A) An atomic model of the F-BAR domain was converted to SPIDER format and filtered to 17 Å (purple) before fitting it manually into the helical reconstruction (grey), confirming that the resolution is at least as good as the *ab inito* estimate (Frank et al., 1996; Sousa and Grigorieff, 2007). B) A windowed region from a raw micrograph of a helical tubule taken at 160kV, revealing a broken open end. C) Representative CTF results from the program ACE (Mallick et al., 2005). D) The final reference projection libraries include images with up to 2° of out-of-plane tilt by 0.15° steps. As the particle images overlap by 97%, a moving average of the out-of-plane

tilt values is plotted against position along the tubule length for two representative tubules.

Figure S3: Fourier-Bessel Reconstructions from Individual Tubules & the Presence of Rotational Symmetry.

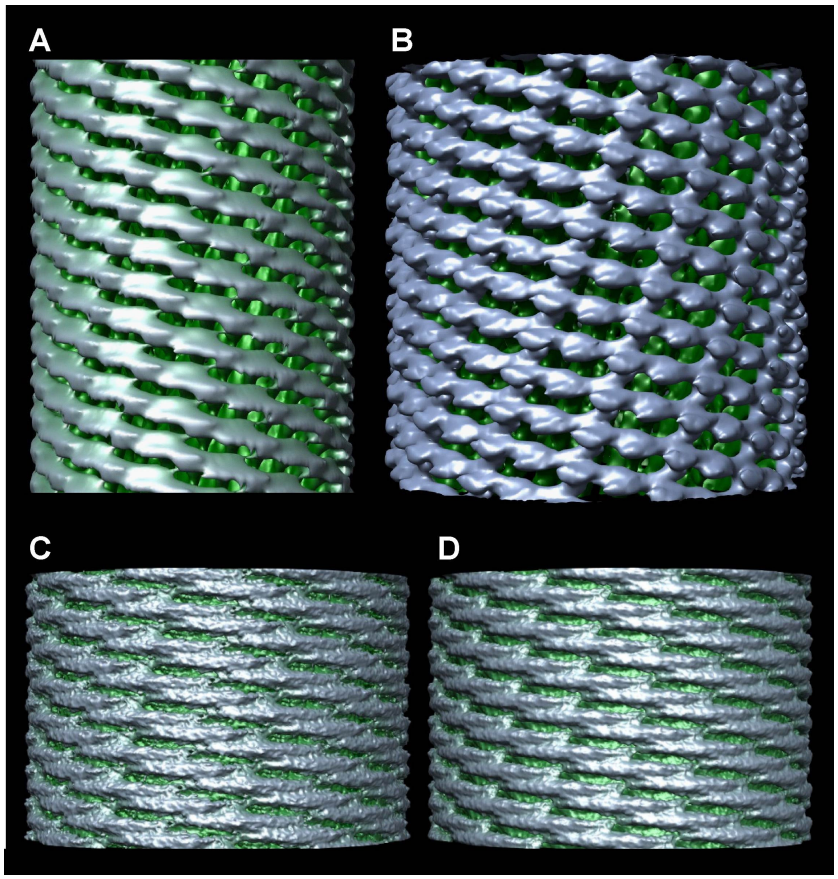

A,B) Volumes calculated via Fourier-Bessel inversion for a narrow (A) and a wide tubule (B) (Carragher et al., 1996). These volumes were used as starting models for single particle iterative helical reconstructions. C,D) The reconstruction shown in Figures 3-4 without (A) versus with (B) imposition of the 2-fold rotational symmetry.

Figure S4: Evolutionary Conservation and Comparison of Electrostatic Surface Potentials of F-BARs from CIP4 and FBP17.

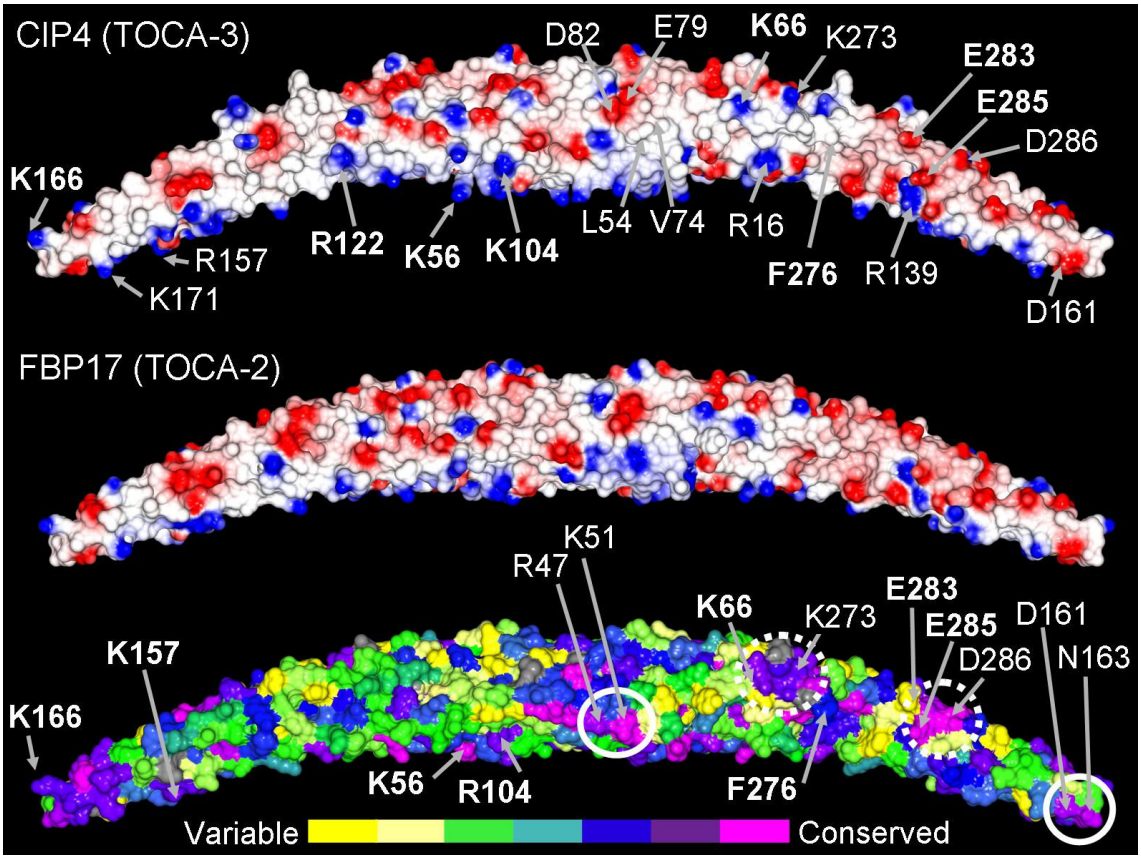

Electrostatic surface potentials for CIP4 (top) and FBP17 (middle) as seen for the lateral surfaces. Surface accessible residues that may participate in either the lateral overlap (right side) or the 'side-lying' interface (left side) are annotated and the residues that were mutated in this study are shown in bold type for the CIP4 surface. The conservation of the FBP17 lateral surface, compared with related members of the Toca family, is shown below. Conservation scores were determined from an alignment of residues 1–300 of human FBP17/TOCA-2 (Q96RU3) with sequences of (accession numbers): human CIP4/TOCA-3 (Q15642), human TOCA-1 (Q5T0N5), Chimpanzee (XP_512320),

Orangutan (Q5RCJ1), Rat (P97531), Mouse (Q8CJ53), *Xenopus tropicalis* (NP_001072662), zebrafish (Q5U3Q6), *Droshophila melanogaster* (NP_65789), and *Caenorhabditis elegans* (NP_741723). The strongest conservation corresponds with surface accessible residues that are likely to laterally interact, as predicted by fitting the F-BAR structures into the helical reconstruction. Solid white circles surround anionic residues at the tip of the module that may interact with cationic residues near the center of the module. Dashed white circles surround anionic and cationic residues that are also likely to interact between laterally-overlapping dimers. A conserved hydrophobic patch, including F276, may also contribute to the laterally-overlapping contacts seen in the helical reconstruction. Finally, residues that appear to constitute the 'side-lying' interface are also conserved, as shown on the left side of the image.

Figure S5: FBP17 F-BAR Mutant Analysis *in vitro*

A) Lower magnification images of samples generated with wild-type protein versus B) the mutant K66E, demonstrating the striking differences in tubule number, length, and rigidity seen *in vitro* and quantified in Figure 6A. C) View of the concave surface of the FBP17 F-BAR domain along the dimer axis with F117 and surrounding residues shown

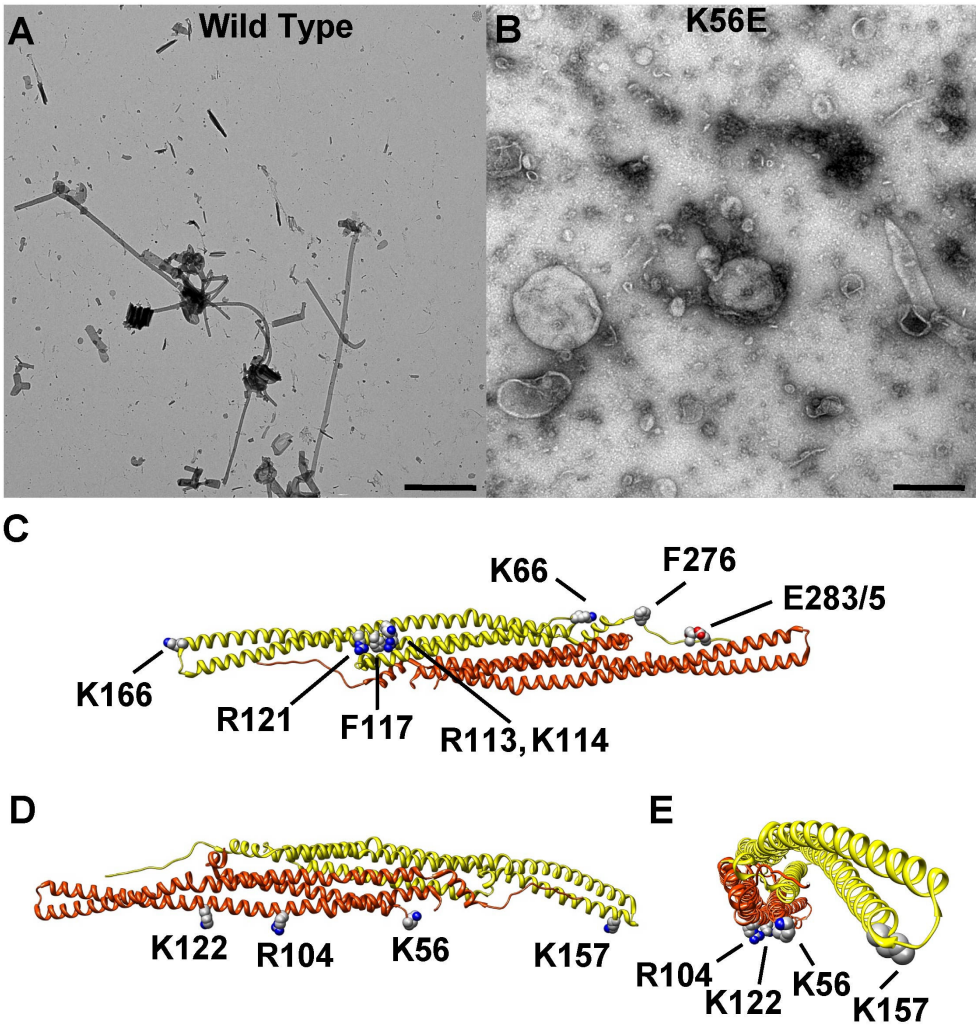

with space-filling atoms. Additional residues mutated in this study are also shown. D) Ribbon diagram of the FBP17 F-BAR domain parallel with the bilayer surface, with the membrane-binding residues that constitute the flat-lattice interface shown with space-

filling atoms. E) Same as 'D' but seen along the module's long axis. Bars (C) 2 μm; (D) 500 nm.

Figure S6: (Cryo)Electron Micrograph of Co-existing Protein-Filaments, Helical and 2D Lattices; Wide Angle X-Ray Scatter of Lipid Samples; Calculated Fourier Transform, and K66E Mutant Phenotype.

A) Electron (cryo)micrograph of protein filaments formed by F-BAR domains (see also

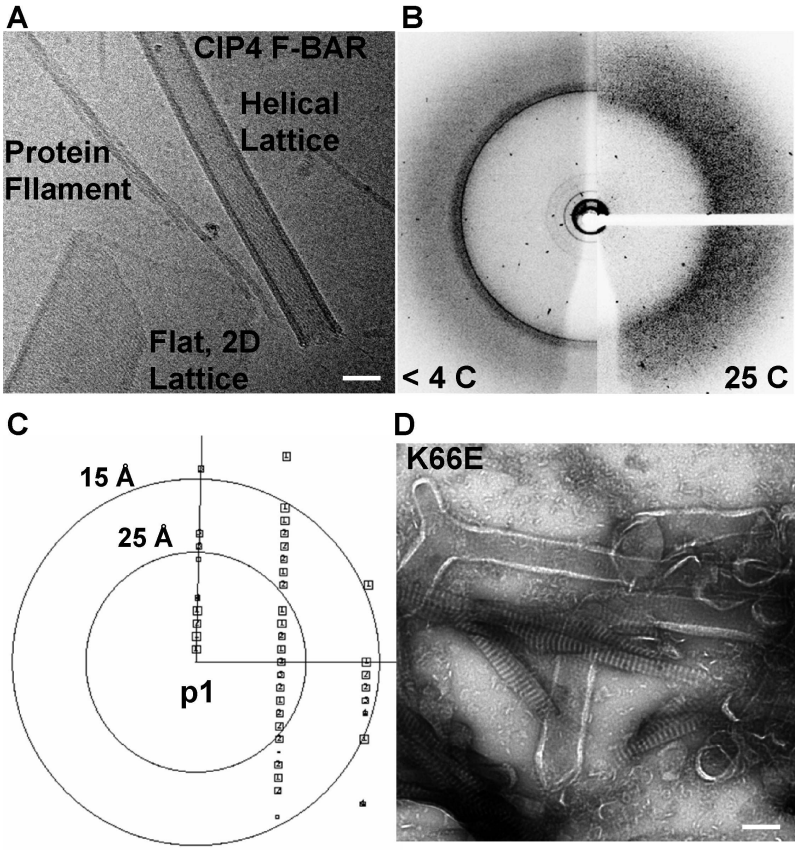

Figure S7) alongside a 2D lattice and a helical tubule, all formed by the same preparation of CIP4 residues 1-284. B) Wide-angle X-ray diffractogram of hydrated liposomes

equilibrated at 25°C (right side) and <4°C (left side). The synthetic lipid mixture used in this study appears to undergo a temperature-dependent phase transition/separation over this range, at approximately 4°C. The sharp ring at ~4.2Å corresponds with the hexagonal packing of acyl chains. C) Phase error of unique reflections to 15Å calculated for the projection terms of the 3D mtz dataset. The size of the boxes in the plot correspond to the phase error associated with each measurement (1, <8°; 2, <14°; 3, <20°; 4, <30°; 5, <40°; 6, <50°; 7, <80°; 8,<90°, where 90° is random). Box size decreases with increasing phase error. D) Negatively stained sample of the K66E mutant incubated with liposomes at RT, showing a mix of tubules, liposomes, and small strips of the 2D lattices. Bars 70 nm.

Figure S7: F-BAR Domains Polymerize into Filaments Composed of Lateral and Tip-to-Tip Interactions.

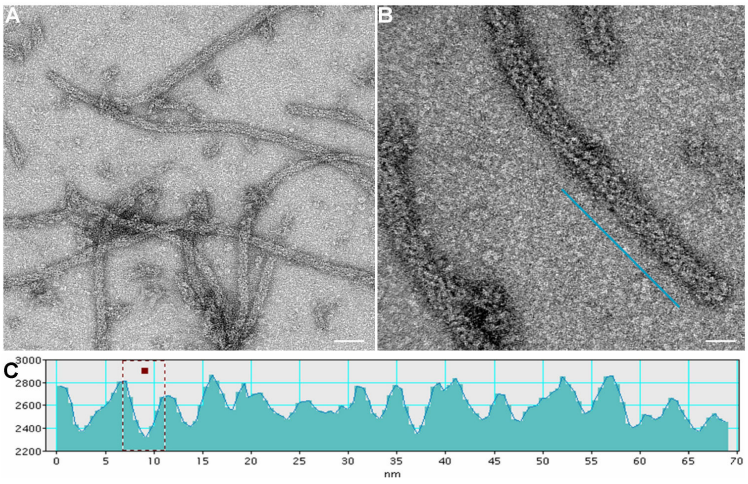

A) Low and B) high power views of negatively stained filaments composed of purified F-BAR domains (CIP4 1 – 284aa) in 100mM NaCl buffered solution without lipids or detergents. C) Pixel values sampled along the center of the filament corresponding with the region indicated by the blue line in 'B' revealing a periodicity of 4-5 nm. Bars (A) 46 nm; (B) 12nm.

Figure S8: Representative Lattice Lines from 2D Crystal Tilt-Series

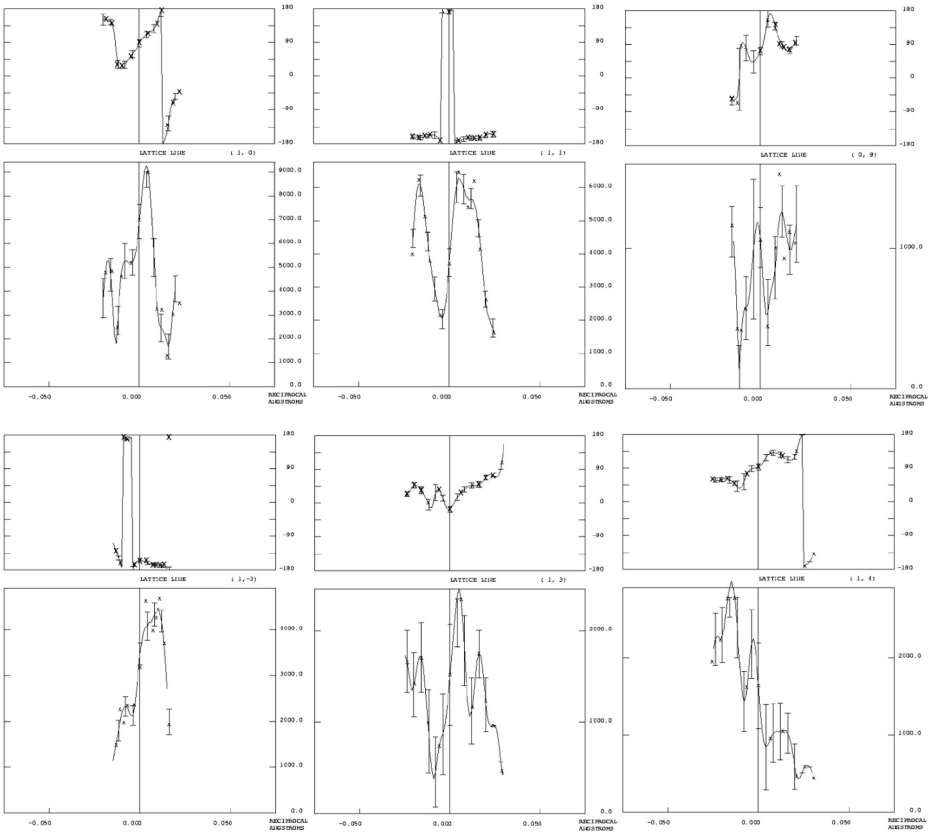

Amplitude and phase variations along representative lattice lines after merging data from tilted crystals in the plane group p1, including all reflections with a signal-to-noise ratio of >4. The continuous curves were computed by the program LATLINE (Crowther et al., 1996). The horizontal z* axis is the distance from the origin of the lattice line. Symbols in the phase plots refer to the quality of the data, as given by IQ values. Error bars are the SD of phases and amplitudes for the fitted structure factors.

Figure S9: Protein-Free Liposome Controls

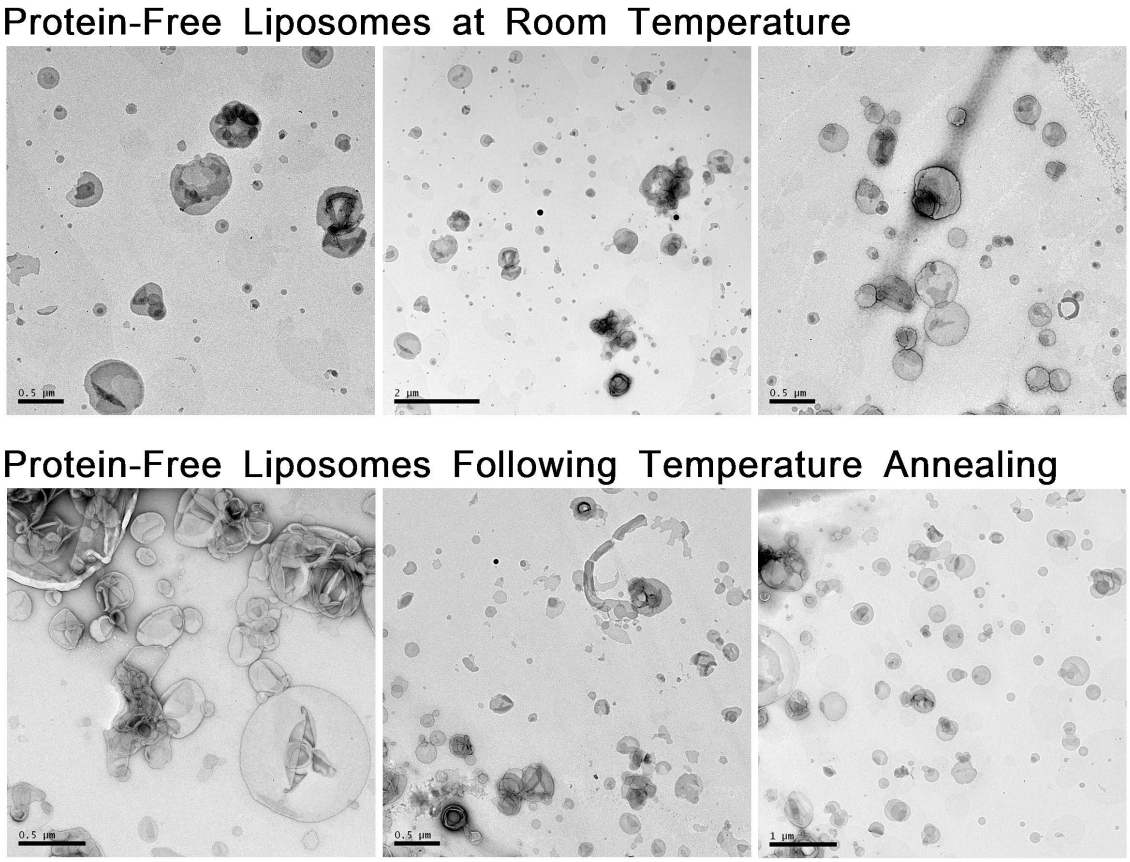

Low magnification images of a typical liposome preparation at RT, prepared by sonication and repeated cycles of freeze-thaw (top panel). Low magnification images of the same lipid preparation subjected to the temperature annealing protocol described here. Occasionally, tubular structures could be seen, but they bore no resemblance to F-BAR induced tubules (bottom panel).

TABLE S1 2D CRYSTAL IMAGE STATISTCS

Unit Cell Parameters (n=6)[1]	a = 32.8±0.4 Å b = 213.9±1.0 Å γ = 91.0±0.6°
Images in Single-Axis Tilt Series	13
Tilt Range	±40°
Range of Defocus	1550-3150 Å
Range of Astigmatism	29-600 Å
Number of Observations[2]	304
Number Fitted Structure Factors	128
Overall weighted phase residual	5.5°

Internal Phase Residual Symmetry Comparisons[3]

		PHASE RESID. COMPAR. vrs. other spots (90° random)		PHASE RESID. SPOTS vrs. Theoretical (45° random)		Target Residuals
1	p1	22.7	66	--	--	
2	p2	59.0	33	29.5	66	37.8
3b	p12_b	58.4	16	36.4	4	27.4
3a	p12_a	57.7	22	41.4	16	30.2
4b	p121_b	59.6	16	33.8	4	27.4
4a	p121_a	52.3	22	25.4	16	30.2
5b	c12_b	58.4	16	36.4	4	27.4
5a	c12_a	57.7	22	41.4	16	30.2
6	p222	61.6	71	29.5	66	31.4
7b	p2221b	61.4	71	31.6	66	31.4
7a	p2221a	63.0	71	34.8	66	31.4
8	p22121	66.0	71	38.4	66	31.4
9	c222	61.6	71	29.5	66	31.4
10	p4	54.3	49	29.9	66	33.9
11	p422	60.6	102	29.5	66	29.7
12	p4212	72.2	102	38.3	66	29.7
13	p3	40.4	20	--	--	25.9
14	p312	49.3	54	28.1	8	26.7
15	p321	58.5	62	39.3	24	28.2
16	p6	61.2	73	29.5	66	31.3
17	p622	63.7	149	37.8	66	28.5

[1] six independent crystals, five imaged after negative staining in 1% uranyl acetate, one imaged under cryo conditions. [2] to 15 Å resolution with $z^* = \pm 0.028$ Å^{-1} [3] Phase residuals were calculated with the program ALLSPACE (Valpuesta et al., 1994). Similar results were obtained for all images of nominally untilted crystals in negative stain and cryo conditions, and for all images obtained within ±10° of tilt.

Supplemental References

Carragher, B., Whittaker, M., and Milligan, R. A. (1996). Helical Processing Using PHOELIX. Journal of Structural Biology *116*, 107-112.

Crowther, R. A., Henderson, R., and Smith, J. M. (1996). MRC image processing programs. J Struct Biol *116*, 9-16.

Derenyi, I., Julicher, F., and Prost, J. (2002). Formation and interaction of membrane tubes. Phys Rev Lett *88*, 238101.

Egelman, E. (2000). A robust algorithm for the reconstruction of helical filaments using single-particle methods. Ultramicroscopy *85*, 225-234.

Frank, J., Radermacher, M., Penczek, P., Zhu, J., Li, Y., Ladjadj, M., and Leith, A. (1996). SPIDER and WEB: processing and visualization of images in 3D electron microscopy and related fields. J Struct Biol *116*, 190-199.

Itoh, T., Erdmann, K., Roux, A., Habermann, B., Werner, H., and De Camilli, P. (2005). Dynamin and the actin cytoskeleton cooperatively regulate plasma membrane invagination by BAR and F-BAR proteins. Dev Cell *9*, 791–804.

Landau, M., Mayrose, I., Rosenberg, Y., Glaser, F., Martz, E., Pupko, T., and Ben-Tal, N. (2005). ConSurf: identification of functional regions in proteins by surface-mapping of phylogenetic information. Nucleic Acids Res *33*, W299-W302.

Le Goff, L., Amblard, F., and Furst, E. M. (2002a). Motor-driven dynamics in actin-myosin networks. Phys Rev Lett *88*, 018101.

Le Goff, L., Hallatschek, O., Frey, E., and Amblard, F. (2002b). Tracer studies on f-actin fluctuations. Phys Rev Lett *89*, 258101.

Mallick, S. P., Carragher, B., Potter, C. S., and Kriegman, D. J. (2005). ACE: Automated CTF Estimation. Ultramicroscopy *104*, 8-29.

Pettersen, E., Goddard, T., Huang, C., Couch, G., Greenblatt, D., Meng, E., and Ferrin, T. (2004). UCSF Chimera—A visualization system for exploratory research and analysis. Journal of Computational Chemistry *25*, 1605-1612.

Pomfret, A. J., Rice, W. J., and Stokes, D. L. (2007). Application of the iterative helical real-space reconstruction method to large membranous tubular crystals of P-type ATPases. J Struct Biol *157*, 106-116.

Potterton, L., McNicholas, S., Krissinel, E., Gruber, J., Cowtan, K., Emsley, P., Murshudov, G., Cohen, S., Perrakis, A., and Noble, M. Developments in the CCP 4 molecular-graphics project. logo *60*, 2288-2294.

Roux, A., Uyhazi, K., Frost, A., and De Camilli, P. (2006). GTP-dependent twisting of dynamin implicates constriction and tension in membrane fission. Nature *441*, 528-531.

Schroeter, J. P., and Bretaudiere, J.-P. (1996). SUPRIM: Easily Modified Image Processing Software. Journal of Structural Biology *116*, 131-137.

Shaw, P., and Hills, G. (1981). Tilted specimen in the electron microscope: a simple specimen holder and the calculation of tilt angles for crystalline specimens. Micron *12*, 279-282.

Smith, J. M. (1999). Ximdisp--A visualization tool to aid structure determination from electron microscope images. J Struct Biol *125*, 223-228.

Sousa, D., and Grigorieff, N. (2007). Ab initio resolution measurement for single particle structures. J Struct Biol *157*, 201-210.
Valpuesta, J. M., Carrascosa, J. L., and Henderson, R. (1994). Analysis of electron microscope images and electron diffraction patterns of thin crystals of phi 29 connectors in ice. J Mol Biol *240*, 281-287.
Whittaker, M., Carragher, B. O., and Milligan, R. A. (1995). PHOELIX: a package for semi-automated helical reconstruction. Ultramicroscopy *58*, 245-259.